



Article

A Robust Nonlinear Filter Strategy Based on Maximum Correntropy Criterion for Multi-GNSS and Dual-Frequency RTK

Jian Liu ¹, Tong Liu ¹ , Yuanfa Ji ², Mengfei Sun ¹, Mingyang Lyu ³, Bing Xu ³ , Zhiping Lu ¹ and Guochang Xu ^{1,*}

¹ Institute of Space Science and Applied Technology, Harbin Institute of Technology (Shenzhen), Shenzhen 518055, China

² Guangxi Key Laboratory of Wireless Broadband Communication and Signal Processing, Guilin 541004, China

³ Department of Aeronautical and Aviation Engineering, The Hong Kong Polytechnic University, Hong Kong SAR, China

* Correspondence: xuguochang@hit.edu.cn

Abstract: The multi-constellation, multi-frequency Global Navigation Satellite System (GNSS) has the potential to empower precise real-time kinematics (RTK) with higher accuracy, availability, continuity, and integrity. However, to enhance the robustness of the nonlinear filter, both the measurement quality and efficiency of parameter estimation need consideration, especially for GNSS challenging or denied environments where outliers and non-Gaussian noise exist. This study proposes a nonlinear Kalman filter with adaptive kernel bandwidth (KBW) based on the maximum correntropy criterion (AMC-KF). The proposed method excavates data features of higher order moments to enhance the robustness against noise. With the wide-lane and ionosphere-free combination, a dual frequency (DF) data-aided ambiguity resolution (AR) method is also derived to improve the measurement quality. The filtering strategy based on the DF data-aided AR method and AMC-KF is applied for multi-GNSS and DF RTK. To evaluate the proposed method, the short baseline test, long baseline test, and triangle network closure test are conducted with DF data from GPS and Galileo. For the short baseline test, the proposed filter strategy could improve the positioning accuracy by more than 30% on E and N components, and 60% on U. The superiority of the proposed adaptive KBW is validated both in efficiency and accuracy. The triangle network closure test shows that the proposed DF data-aided AR method could achieve a success rate of more than 93%. For the long baseline test, the integration of the above methods gains more than 40% positioning accuracy improvement on ENU components. This study shows that the proposed nonlinear strategy could enhance both robustness and accuracy without the assistance of external sensors and is applicable for multi-GNSS and dual-frequency RTK.

Keywords: multi-GNSS; real-time kinematic; maximum correntropy criterion; Kalman filter; wide-lane; ionosphere-free



Citation: Liu, J.; Liu, T.; Ji, Y.; Sun, M.; Lyu, M.; Xu, B.; Lu, Z.; Xu, G. A Robust Nonlinear Filter Strategy Based on Maximum Correntropy Criterion for Multi-GNSS and Dual-Frequency RTK. *Remote Sens.* **2022**, *14*, 4578. <https://doi.org/10.3390/rs14184578>

Academic Editor: Giuseppe Casula

Received: 30 July 2022

Accepted: 9 September 2022

Published: 13 September 2022

Publisher's Note: MDPI stays neutral with regard to jurisdictional claims in published maps and institutional affiliations.



Copyright: © 2022 by the authors. Licensee MDPI, Basel, Switzerland. This article is an open access article distributed under the terms and conditions of the Creative Commons Attribution (CC BY) license (<https://creativecommons.org/licenses/by/4.0/>).

1. Introduction

The current operating Global Navigation Satellite System (GNSS) includes the Global Positioning System (GPS), Globalnaya Navigazionnaya Sputnikovaya Sistema (GLONASS), BeiDou (BDS), and Galileo. The precise position, velocity, and time (PVT) generated from real-time kinematics (RTK) are crucial for engineering surveys, fleet monitoring, intelligent transportation systems, geographical information systems, guidance and control, etc. [1,2]. By 2024, more than 110 satellites with different frequencies are expected to be accessible for multi-GNSS. Compared with a single constellation, multiple constellations and frequencies could improve the accuracy, continuity, availability, and integrity significantly [3], while enhancing the robustness against noise and outliers [4].

Multi-GNSS applications usually apply loosely and tightly coupled models for data curation [5,6]. Both of them could achieve similar performance [7] in precise point positioning [8] and multi-sensor fusion such as integrating GNSS with the Inertial Navigation

System, Simultaneous Location and Mapping, Lidar, and 5G [9–15]. Although the tightly coupled model shares one common pivot satellite for each constellation, it is challenging to improve the model strength due to the presence of double difference inter-system bias (DISB) originating from receivers [16]. In this study, the loosely coupled model is used due to its usability [17].

Even if dual-frequency (DF) data is available [18–20], the ambiguity resolution is still impacted in urban environments due to signal blockage and interference [18–21]. The traditional extended Kalman filter is sensitive to outliers and noise [22], as it is based on the second-order statistics (e.g., variance, correlation, etc.) that exist in the Gaussian noise assumption and minimum mean square error (MSE) criterion [23]. Thus, the following limitations still need to be addressed: (1) The unmodeled non-Gaussian noise and heavy-tail noise originated not only from the outliers and gross errors but also the missed data due to signal blockage and deformation [24]. (2) The lack of complete prior knowledge of system dynamics and observations may eventually cause divergence [25]. Extensive attempts have been made to address these problems. One solution is the particle filter (PF), which is capable of estimating the posterior probability density function (PDF) by massive particles [26]. Multi-model filters such as the Gaussian sum filter (GSF) are another solution, which parallelly implement and interactively combine several filters to estimate the system states. A computationally economical filter was studied by integrating the robust M estimation into the GSF framework [27]. Heavy-tailed distribution-based filters and the H_∞ filter have also been studied in [28]. However, attention still needs to be paid, as most of them are deficient in universality and efficiency [29].

Recently, correntropy has received growing attention in signal processing, posture estimation, and machine learning [30–33]. It is a measurable metric of local similarity and is established on Gaussian kernel functions. Specifically, higher dimensional data matching and error detection can be realized, as Gaussian kernel functions enrich data features by transforming the observation into the Hilbert space with higher dimensions. Thus, the maximum correntropy between the input and output is robust against various types of noise and even arbitrarily large outliers, and can be achieved according to the maximum correntropy criterion (MCC). Although the kernel bandwidth (KBW) is the key parameter for implementing the MCC, existing studies mostly treat it as an exogenous parameter from empirical experiments, rather than an endogenous variable of the system [33–36]. In this paper, a nonlinear adaptive Kalman filter (KF) based on MCC with adaptive KBW is proposed. The Gaussian hypothesis and MSE criterion are further relaxed, which aims to improve the adaptability and robustness [37]. The main contributions of the proposed method are: (1) The AMC-KF is proposed as a new robust nonlinear filter to improve the precision and robustness of multi-GNSS DF RTK [38]. (2) The DF data-aided AR method is proposed to fix ambiguities with the wide-lane and ionosphere-free combinations. The wide-lane pseudo-range is introduced for medium and long baseline RTK. (3) A nonlinear filter strategy is designed by integrating the DF data-aided AR method into the proposed AMC-KF. The test results show the significant superiority of the proposed strategy with various baselines.

The remainder of this paper is organized as follows: In Section 2, the double difference (DD) RTK model is introduced, followed by the derivation of the proposed DF data-aided AR method. The loosely coupled model for multi-GNSS is also presented. In Section 3, correntropy is introduced and the AMC-KF is elaborated in detail. Moreover, the derivation of the adaptive KBW is outlined. In Section 4, the performance of the proposed filter strategy is demonstrated. Datasets collected from the continuously operating reference stations (CORS) network of Australia are used for the short baseline test, adaptive strategy test, and the long baseline test. Finally, some conclusions are given in Section 5.

2. RTK Mathematic Model

2.1. Constrained Loosely Coupled Model

The DD carrier phase measurement φ (in cycles) with wavelength λ and code measurement P (in meters) is defined as follows [1]:

$$\begin{cases} \lambda \nabla \Delta \varphi = \nabla \Delta \rho - \lambda \nabla \Delta N + \nabla \Delta T - \nabla \Delta I + \nabla \Delta \varepsilon \\ \nabla \Delta P = \nabla \Delta \rho + \nabla \Delta T + \nabla \Delta I + \nabla \Delta \xi \end{cases} \quad (1)$$

where $\nabla \Delta$ is the DD operator; ρ , T , I , and N are the receiver-satellite geometric range, tropospheric delay, ionospheric delay, and carrier phase ambiguity, respectively; and ξ and ε are the unmodeled errors including multipath noise, system noise, etc. The covariance matrix of the system state, system noise, measurement noise, and design matrices can be defined as P , Q , R , and H . The filter-state vector consists of positioning information and the DD ambiguities can be expressed as [7]:

$$\mathbf{x} = [x_n^G \quad x_u^G \quad x_e^G \quad x_e^G \quad x_n^G \quad x_u^G \quad \nabla \Delta N^G \quad \nabla \Delta N^E]^T$$

where the superscripts 'G' and 'E' represent GPS and Galileo, and the subscripts e , n , and u represent different directions. The $\text{diag}(\cdot)$ is a diagonal matrix. The KF recursive process is defined as [1]:

$$\left. \begin{cases} \hat{\mathbf{x}}_{k|k-1} = \mathbf{F}_{k,k-1} \hat{\mathbf{x}}_{k-1} \\ \mathbf{P}_{k|k-1} = \mathbf{F}_{k,k-1} \mathbf{P}_{k-1} \mathbf{F}_{k,k-1}^T + \mathbf{\Gamma}_{k-1} \mathbf{Q}_{k-1} \mathbf{\Gamma}_{k-1}^T \\ \mathbf{P}_k = (\mathbf{I} - \mathbf{K}_k \mathbf{H}_k) \mathbf{P}_{k|k-1} \\ \mathbf{K}_k = \mathbf{P}_{k|k-1} \mathbf{H}_k^T (\mathbf{H}_k \mathbf{P}_{k|k-1} \mathbf{H}_k^T + \mathbf{R}_k)^{-1} \\ \hat{\mathbf{x}}_k = \hat{\mathbf{x}}_{k|k-1} + \mathbf{K}_k (\mathbf{z}_k - \mathbf{H}_k \hat{\mathbf{x}}_{k|k-1}) \end{cases} \right\} \begin{array}{l} \text{prediction} \\ \text{update} \end{array} \quad (2)$$

where K , F are the gain and state transform matrix; and \mathbf{z}_k and \mathbf{x}_k are the measurements and state that needs to be estimated at the k th epoch. As $x_G = x_E$ once successfully located, the following constraint can be attached [39]:

$$\underbrace{\begin{bmatrix} \mathbf{I}_{3 \times 3} & -\mathbf{I}_{3 \times 3} \end{bmatrix}}_D \underbrace{\begin{bmatrix} x_G \\ x_E \end{bmatrix}}_X = \underbrace{\begin{bmatrix} 0_{3 \times 3} \end{bmatrix}}_M \quad (3)$$

where \mathbf{I} represents the unit matrix, and D and M are the constraint matrices. The prediction step in (2) can be developed to constrain KF as follows:

$$\begin{cases} \mathbf{x}_{k|k-1} = \mathbf{x}_{k|k-1} - \mathbf{D}_k^T (\mathbf{D}_k \mathbf{D}_k^T)^{-1} (\mathbf{D}_k \mathbf{D}_k^T)^{-1} (\mathbf{D}_k \mathbf{x}_{k|k-1} - \mathbf{M}_k) \\ \mathbf{P}_{k|k-1} = (\mathbf{I} - \mathbf{D}_k^T (\mathbf{D}_k \mathbf{D}_k^T)^{-1} \mathbf{D}_k)^T \mathbf{P}_{k|k-1} (\mathbf{I} - \mathbf{D}_k^T (\mathbf{D}_k \mathbf{D}_k^T)^{-1} \mathbf{D}_k) \end{cases} \quad (4)$$

2.2. DF Data-Aided AR

Defining N_1 and N_2 as the carrier ambiguities on frequencies f_1 and f_2 , respectively, the ρ on different frequencies can be formed by $\nabla \Delta \varphi$ as follows:

$$\begin{cases} \nabla \Delta \rho_1 = (\nabla \Delta \varphi_1 + \nabla \Delta N_1) \lambda_1 - \frac{A}{f_1^2} \\ \nabla \Delta \rho_2 = (\nabla \Delta \varphi_2 + \nabla \Delta N_2) \lambda_2 - \frac{A}{f_2^2} \end{cases} \quad (5)$$

where N_e is the number of electrons in unit area $A = 40.3 \int_S N_e ds$. The wide-lane ambiguity $\nabla \Delta N_w$ with wavelength λ_w can be expressed as:

$$\nabla \Delta N_w = \nabla \Delta \varphi_1 - \nabla \Delta \varphi_2 - \frac{1}{\lambda_w} \left(\nabla \Delta \rho - \nabla \Delta T - \frac{f_1}{f_2} \nabla \Delta I - \nabla \Delta \varepsilon \right) \quad (6)$$

For the atmosphere errors in the above equation, $\nabla\Delta I$ cannot be ignored for long baselines due to the spatial difference. $\nabla\Delta T$ varies from 2 to 20 m depending on the satellite elevation, but a higher cutoff angle reduces data utilization [40]. Thus, the timeliness of the fixed solution could not be guaranteed, which is crucial for dynamic RTK once the satellites are available [41–44]. The proposed DF data-aided AR method is summarized as follows:

$$\begin{cases} \nabla\Delta N_w = (\nabla\Delta\varphi_1 - \nabla\Delta\varphi_2) - \frac{(f_1\nabla\Delta P_1 + f_2\nabla\Delta P_2)}{\lambda_w(f_1 + f_2)} + \nabla\Delta\varepsilon \\ \nabla\Delta N_1 = \frac{1}{m\lambda_1 - n\lambda_2} [\nabla\Delta\varphi_{IF} - m\nabla\Delta\varphi_1 + n\nabla\Delta\varphi_2 - n\lambda_2\nabla\Delta N_w] \\ \nabla\Delta N_2 = \nabla\Delta N_1 - \nabla\Delta N_w \end{cases} \quad (7)$$

where $\nabla\Delta\varphi_{IF}$ is the ionosphere-free combination for carrier observations, $m = \frac{f_1^2}{f_1^2 - f_2^2}$ and $n = \frac{f_2^2}{f_1^2 - f_2^2}$, and $\nabla\Delta\varepsilon$ represents the noise. The above method introduces the code wide-lane combination to invert $\nabla\Delta N_1$ and the derivation can be found in Appendices A and B. The proposed method shows the following merits: (1) The positioning accuracy and AR success rate are improved as the influence of $\nabla\Delta I$ error is eliminated. (2) The method is applicable for medium and long baselines as the limitation of geometry distance ρ is eliminated. (3) The $\nabla\Delta N$ on each frequency can be inverted directly from the high precise ionosphere-free and wide-lane measurements. Moreover, the following moving average with n epochs is also adopted to reduce the effect result from noise in $\nabla\Delta P$ [45]:

$$\nabla\Delta\hat{N}_w(n) = \frac{\sum_{i=k}^{k+n} Z^i \nabla\Delta N_w^i}{\sum_{i=k}^{k+n} Z^i} \quad (8)$$

where k is the start epoch of the observation arc without cycle slip. Z^i is the weight of i th epoch. The $\nabla\Delta\hat{N}_w(n)$ could be fixed to $\text{round}(\nabla\Delta\hat{N}_w(n))$ by the integer rounding method [46] if the differential residual of $\nabla\Delta\hat{N}_w$ between adjacent epochs meets the following constraint:

$$|\nabla\Delta\hat{N}_w(n) - \nabla\Delta\hat{N}_w(n - 1)| < 0.1 \text{ cycles}$$

Then, the corresponding $\nabla\Delta N_1$, $\nabla\Delta N_2$ and precise carrier measurements could be formed by Equation (7). In the following test, the moving average window width n is set to be five epochs.

3. AMC-KF

The obtained $\nabla\Delta N_1$ and $\nabla\Delta N_2$ could be applied to form precise $\nabla\Delta\varphi$ in Equation (1), and used for state estimating in the nonlinear filter.

3.1. KF Based on MCC Derivation

Assuming the joint PDF of random variables X and Y as $F_{XY}(x,y)$, the correntropy is defined as follows [47]:

$$\begin{aligned} V(X, Y) &= E[G_\sigma(X - Y)] \\ &= \int G_\sigma(x - y) dF_{XY}(x, y) \\ &= \int \exp\left(-\frac{(X - Y)^2}{2\sigma^2}\right) dF_{XY}(x, y) \end{aligned} \quad (9)$$

where σ is the KBW, E is the expectation operator, and G_σ is the non-negative Gaussian kernel function. Furthermore, the Taylor expansion of the above equation is:

$$V(X, Y) = \frac{1}{\sqrt{2\pi}\sigma} \sum_{n=0}^{\infty} \frac{(-1)^n}{2^n n!} E\left[\frac{(X - Y)^{2n}}{\sigma^{2n}}\right] \quad (10)$$

Here, V is essentially a correlation function in the local kernel space controlled by σ , as it is the weighted sum of all even order moments of $(X-Y)$. This localization proves meaningful in measuring the similarity between X and Y [48,49]. Then, the KF based on MCC (MCC-KF) can be established by optimizing the following loss function [50–52]:

$$J_C = G_\sigma(\|z_k - H\hat{x}_k\|) + G_\sigma(\|\hat{x}_k - \Phi\hat{x}_{k-1}\|) \tag{11}$$

where $\| \cdot \|$ denotes the Euclidean norm. J_C is only a function of σ [25]. Let $\frac{\partial J_C}{\partial \hat{x}_k} = 0$; the estimated state can be obtained as follows [53]:

$$\hat{x}_k = \Phi\hat{x}_{k-1} + \frac{G_\sigma(\|z_k - H\hat{x}_k\|)}{G_\sigma(\|\hat{x}_k - \Phi\hat{x}_{k-1}\|)} H^T(z_k - H\hat{x}_k) \tag{12}$$

It tells that the MCC will be achieved if $X = Y$, as G_σ reaches the upper bound and the PDF of the predicted value and the measured value matched to the maximum extent [54]. The further results can be obtained while $x_k \approx F\hat{x}_{k-1}$:

$$\hat{x}_k = \hat{x}_k^- + G_\sigma(\|z_k - H\hat{x}_k\|)H^T(z_k - H\hat{x}_k) \tag{13}$$

3.2. AMC-KF Derivation

The KBW of the originally proposed MCC shown in Equation (13) is usually predefined empirically, which results in the compromise between fast learning initially and fast learning near the optimum point. To derive an adaptive KBW, the loss function is further enhanced as follows:

$$\begin{aligned} J_C &= G_\sigma\left(\|z_k - H\hat{x}_k\|_{R^{-1}}\right) + G_\sigma\left(\|\hat{x}_k - \Phi\hat{x}_{k-1}\|_{P_{k|k-1}^{-1}}\right) \\ &\leq G_\sigma\left(\|z_k - H\hat{x}_k\|_{R^{-1}}\right) + \Lambda \\ &= \frac{1}{N\sqrt{2\pi}\sigma} \sum_{i=n-N+1}^n \exp\left(-\frac{\|z_k - H\hat{x}_k\|_{R^{-1}}^2}{2\sigma^2}\right) + \Lambda \end{aligned} \tag{14}$$

where Λ is a constant overbounded by $\lim_{\|\hat{x}_k - \Phi\hat{x}_{k-1}\|_{P_{k|k-1}^{-1}} \rightarrow 0} G_\sigma\left(\|\hat{x}_k - \Phi\hat{x}_{k-1}\|_{P_{k|k-1}^{-1}}\right)$ [47,55].

To search for the proper σ , the gradient ascent approach is applied by taking a small step μ along the positive gradient, then the n th iteration can be expressed as $\sigma_{n+1} = \sigma_n + \mu \nabla J_C$ [47]. The J_C can be minimized as follows:

$$\begin{aligned} \nabla J_C &= \frac{\partial J_C}{\partial \sigma} = -\frac{1}{N\sqrt{2\pi}\sigma^2} \sum_{i=n-N+1}^n \exp\left(-\frac{\|z_k - H\hat{x}_k\|_{R^{-1}}}{2\sigma^2}\right) + \frac{1}{N\sqrt{2\pi}\sigma} \sum_{i=n-N+1}^n \left(\frac{\|z_k - H\hat{x}_k\|_{R^{-1}}}{\sigma^3}\right) \exp\left(-\frac{\|z_k - H\hat{x}_k\|_{R^{-1}}}{2\sigma^2}\right) \\ &= -\frac{1}{\sqrt{2\pi}\sigma^2} \exp\left(-\frac{\|z_k - H\hat{x}_k\|_{R^{-1}}}{2\sigma^2}\right) + \frac{\|z_k - H\hat{x}_k\|_{R^{-1}}}{\sqrt{2\pi}\sigma^4} \exp\left(-\frac{\|z_k - H\hat{x}_k\|_{R^{-1}}}{2\sigma^2}\right) \\ &= 0 \end{aligned}$$

Then, the closed-form KBW, which can adaptively adjust according to R , is expressed as follows:

$$\sigma = \sqrt{\frac{\|z_k - H\hat{x}_k\|_{R^{-1}}}{2} + \sigma'} \tag{15}$$

Through Equations (4), (12), (13) and (15), the proposed AMC-KF is finally obtained. It should be noted that the exponential part of AMC-KF reduces to constant and is no longer correntropy-based if Equation (15) is applied without the small penalty term σ' . The penalty term is artificially added and can be determined according to [56].

3.3. Filter Implementation

The procedure of the proposed nonlinear strategy is summarized as follows: (1) Removing the ambiguities $\nabla \Delta N$ on each frequency by the DF data-aided AR method. A

threshold and moving average operation are applied to ensure stability and reduce noise. (2) The precise $\nabla\Delta\varphi$ without ambiguities is fed into the AMC-KF for multi-GNSS float solution. The adaptive KBW is used for the prediction and update step during the filtering. Both of them help improve the robustness and accuracy of the float solution. (3) To keep consistency with other RTK structures, the least square ambiguity decorrelation adjustment (LAMBDA) is adopted to transfer the float solution to the fixed solution.

To initialize the proposed filter, the variance-covariance matrix is deduced by the least square method (LS) at the initial epoch. The F and Q can be defined as an identity matrix and a zero matrix without cycle slips. The noise level for non-difference code and carrier measurements are set to 3 m and 3 cm, respectively [1]. The framework of the proposed nonlinear strategy is depicted in Figure 1. As shown in Equation (8), the window width of the moving average and the threshold in the ‘DF Data-aid AR Stage’ is usually set to 5 epochs and 0.1 cycles, which implies the influence on the first time to fix ambiguity is tiny and controllable.

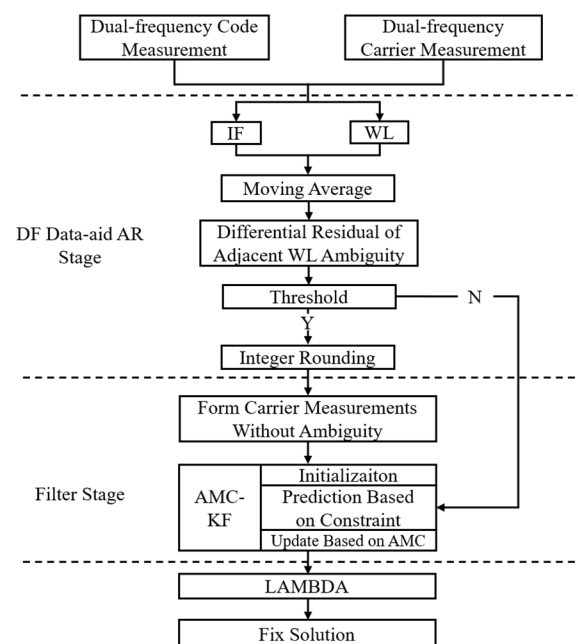


Figure 1. The procedure of the filter implementation.

4. Test and Result

To validate the proposed filter strategy, short and long baseline tests are conducted and the traditional DD KF (DD-KF) model mentioned in [1] is also used for comparison. The DD-KF is established in Equations (1)–(4) without the ‘DF Data-aid AR Stage’. As the noise of original observations is significantly less than those of wide-lane and ionosphere-free combined measurements, thus, the DF Data-aid AR method is not enabled for the short baseline test. The improvements illustrated in the short baseline test are only beneficial from the AMC-KF method. For the long baseline, the DF Data-aid AR stage is enabled to eliminate atmosphere errors; thus, the improvements in the long baseline test are beneficial both from the AMC-KF and the DF Data-aid AR method. All results obtained are based on post-processing performed on an Intel Core i7 2.30 GHz notebook with 16 GB RAM running on Windows 10.

As Figure 2 shows, the dataset is collected from seven Australia CORS stations (BONE, QCLF, ANGS, STNY, NEWH, GSBN, WBEE) on January 1, 2021, and all formed baselines are elaborated in Table 1. The first six baselines range from 19–60 km and are used for the short baseline test. The last two baselines are formed by (BONE, GSBN, WBEE) and used for long baselines. The sample interval and cut-off elevation for all tests are 30 s and 10° , respectively.

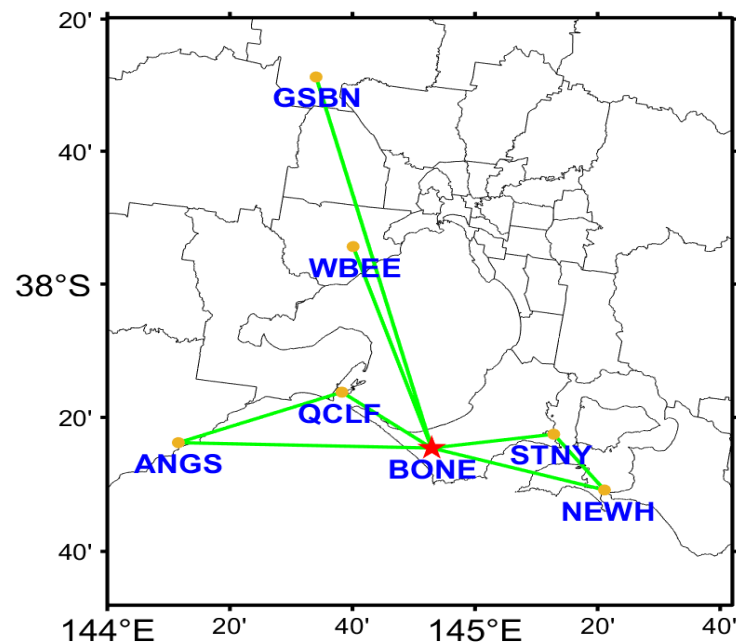


Figure 2. Distribution of CORS station BONE, QCLF, ANGS, STNY, NEWH, GSBN, WBEE. (<https://gnss.ga.gov.au/network> (accessed on 1 January 2021)).

Table 1. Information for different baselines.

No.	Baseline	Distance (km)	Sample Interval	Cut-Off Elevation	Processing Model
1	STNY-NEWH	19.562	30 s	10°	AMC-KF, DD-KF
2	BONE-QCLF	26.363	30 s	10°	AMC-KF, DD-KF
3	BONE-STNY	29.231	30 s	10°	AMC-KF, DD-KF
4	QCLF-ANGS	41.335	30 s	10°	AMC-KF, DD-KF
5	NEWH-BONE	42.606	30 s	10°	AMC-KF, DD-KF
6	ANGS-BONE	60.213	30 s	10°	AMC-KF, DD-KF
7	BONE-WBEE	58.942	30 s	10°	AMC-KF, DD-KF
8	BONE-GSBN	106.877	30 s	10°	AMC-KF, DD-KF

4.1. Position Accuracy Test

Figure 3 depicts the available satellites and the relative dilution of the precision (RDOP) on BONE. The other stations will obtain similar indicators for the short baseline. The average available satellites for filtering in the whole day are 6 for GPS, 6 for Galileo, and 10 for GPS+Galileo. The RDOP for GPS+Galileo is 0.7228 and indicates an ideal environment for relative positioning [1]. If the available satellite number of Galileo is less than four, the position result is obtained only by GPS.

The root mean square (RMS) and standard deviation (STD) of positioning errors on the East (E), North (N), and Up (U) components are shown in Table 2, where the positive and negative values represent improvement and degradation.

For AMC-KF, the RMS on BONE-QCLF, QCLF-ANGS and ANGS-BONE is (0.13417 m, 0.20254 m, 0.30294 m), (0.09421 m, 0.17402 m, 0.27439 m), (0.16395 m, 0.18714 m, 0.26284 m), respectively. While the RMS for DD-KF is (0.28258 m, 0.43671 m, 0.80099 m), (0.23641 m, 0.23035 m, 0.96756 m), (0.53574 m, 0.15190 m, 0.65454 m). The accuracy improvement by (+52.52%, +53.62%, +62.18%), (+60.15%, +24.45%, +71.64%), (+69.40%, −23.20%, +59.84%) is achieved for AMC-KF. Similarly, the STD on each baseline for AMC-KF is (0.10886 m, 0.18606 m, 0.30278 m), (0.08226 m, 0.16659 m, 0.26107 m) and (0.16027 m, 0.16694 m, 0.24867 m) while for DD-KF is (0.10066 m, 0.33062 m, 0.40077 m), (0.11478 m, 0.17340 m, 0.52163 m), (0.23124 m, 0.10958 m, 0.53847 m). AMC-KF ameliorates the performance by (−8.15%, +43.72%, +24.45%), (+28.33%, +3.93%, +49.95%), (+30.69%, −52.35%, +53.82%).

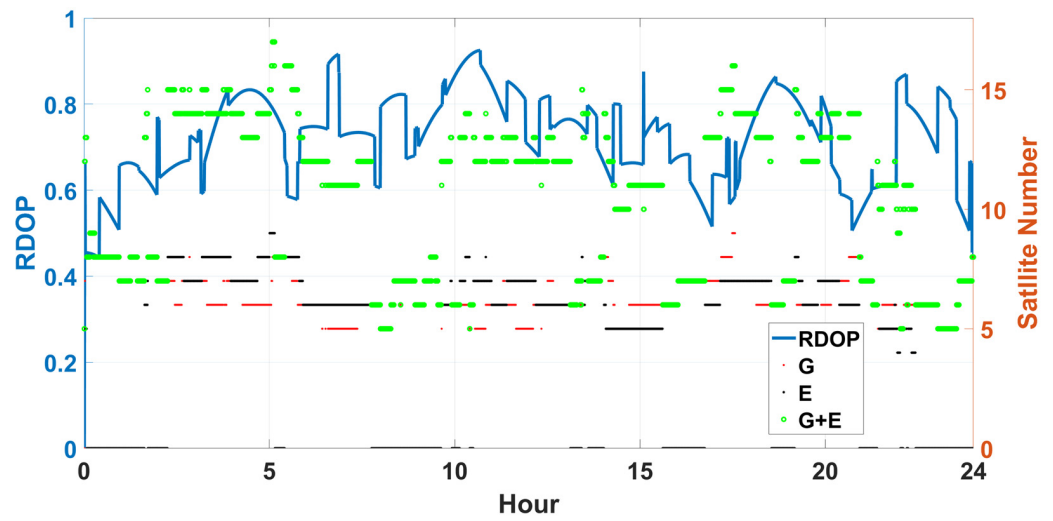


Figure 3. RODP and available satellites of BONE.

For BONE-STNY, STNY-NEWH, NEWH-BONE, the AMC-KF possesses an RMS improvement by (+55.90%, +64.82%, +85.24%), (−22.94%, +60.42%, +83.79%), (+53.43%, +82.67%, +67.43%), and an STD improvement by (+31.55%, +46.827%, +78.57%), (−11.22%, +35.33%, +53.71%) and (+47.26%, +73.50%, +66.16%), respectively.

Compared to DD-KF in each direction, the proposed AMC-KF obtains an improvement by (32.24%, 34.48%, 63.07%) on average, despite negative values existing. Thus, AMC-KF is a beneficial scheme for short baseline RTK as it retains a low-level positioning error. Particularly, the positioning errors on U are reduced by more than 60%. One possible reason for the negative values is that AMC-KF also redistributes the positioning residual since errors in different directions are coupled [57].

Table 2. RMS and STD improvement on ENU for BONE-QCLF-ANGS-BONE.

	Baseline	E		N		U		Improvement on ENU
		AMC-KF	DD-KF	AMC-KF	DD-KF	AMC-KF	DD-KF	
RMSE (m)	BONE-QCLF	0.13417	0.28258	0.20254	0.43671	0.30294	0.80099	+52.52%, +53.62%, +62.18%
	QCLF-ANGS	0.09421	0.23641	0.17402	0.23035	0.27439	0.96756	+60.15%, +24.45%, +71.64%
	ANGS-BONE	0.16395	0.53574	0.18714	0.15190	0.26284	0.65454	+69.40%, −23.20%, +59.84%
STD (m)	BONE-QCLF	0.10886	0.10066	0.18606	0.33062	0.30278	0.40077	−8.15%, +43.72%, +24.45%
	QCLF-ANGS	0.08226	0.11478	0.16659	0.17340	0.26107	0.52163	+28.33%, +3.93%, +49.95%
	ANGS-BONE	0.16027	0.23124	0.16694	0.10958	0.24867	0.53847	+30.69%, −52.35%, +53.82%
RMSE (m)	BONE-STNY	0.15830	0.35895	0.15017	0.42681	0.19493	1.32102	+55.90%, +64.82%, +85.24%
	STNY-NEWH	0.13166	0.10709	0.13620	0.34410	0.19730	1.21688	−22.94%, +60.42%, +83.79%
	NEWH-BONE	0.17273	0.37092	0.13468	0.77698	0.19800	0.60796	+53.43%, +82.67%, +67.43%
STD (m)	BONE-STNY	0.13460	0.19663	0.14762	0.27757	0.18249	0.85175	+31.55%, +46.827%, +78.57%
	STNY-NEWH	0.11695	0.10515	0.13590	0.21013	0.19655	0.42460	−11.22%, +35.33%, +53.71%
	NEWH-BONE	0.10496	0.19900	0.13333	0.50321	0.19746	0.58359	+47.26%, +73.50%, +66.16%

4.2. Adaptive Strategy Test

The variation and statistics of KBW are shown in Figure 4. The AMC-KF is proved to be effective as the KBW increases rapidly after initialization to respond to the input GNSS measurements and varies epoch by epoch. In Figure 4b, the mean and standard deviation found for (STNY-NEWH, QCLF-ANGS, NEWH-BONE, BONE-STNY, BONE-

QCLF) are (16.1284, 14.9827, 20.6101, 19.1174, 13.1624, 17.0062) and (4.7120, 5.1061, 6.1030, 5.4980, 3.9002, 5.38731), respectively. Although the KBW is different from each other as all baselines are spatially separated, the similar variation trend verified that the adaptive KBW is sensitive to the environment.

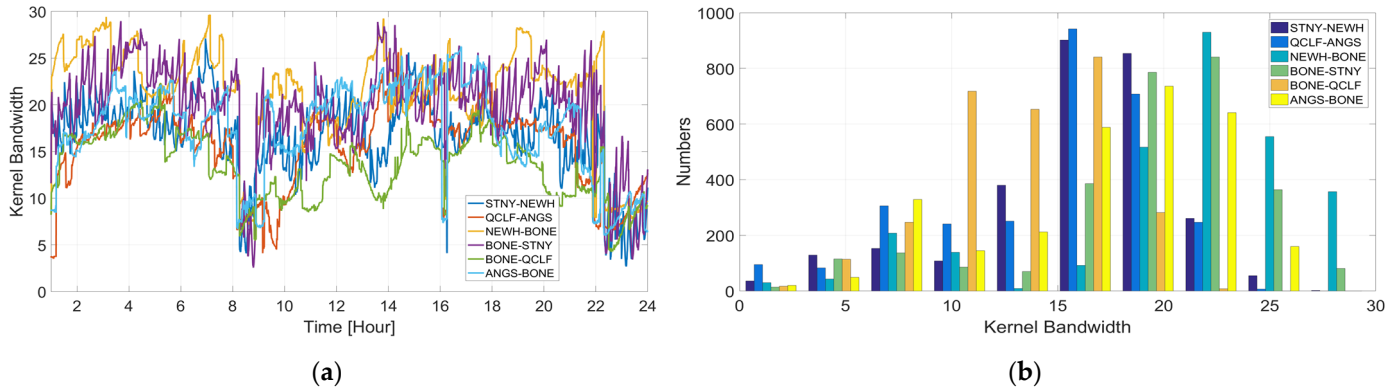


Figure 4. KBW time series and statistics for each baseline. (a) Time series for each baseline; (b) the statistics of KBW time series.

The filter time consumption with the proposed adaptive KBW and the original fixed KBW in MCC is illustrated in Figures 5 and 6. The fixed KBW used here is set to be 1, 5, 25, and 30, as all KBW has shown in Figure 4b fall in [0, 30].

It could be found that the adaptive KBW owns smoother and more stable processing results. It means that the embedded devices and on-chip modules may benefit from power conservation [1]. For adaptive KBW, the average time consumption at each epoch is (0.0683 s, 0.0535 s, 0.0520 s, 0.0674 s, 0.0641 s, 0.0495 s) on ANGS-BONE, BONE-QCLF, BONE-STNY, NEWH-BONE, QCLF-ANGS, STNY-NEWH. While for fixed KBW (1, 5, 25, 30) are (0.0619 s, 0.0599 s, 0.0717 s, 0.0659 s), (0.0528 s, 0.0549 s, 0.0517 s, 0.0544 s), (0.0515 s, 0.0543 s, 0.0581 s, 0.0582 s), (0.0542 s, 0.0681 s, 0.0680 s, 0.0543 s), (0.0658 s, 0.0594 s, 0.0679 s, 0.0662 s) and (0.0581 s, 0.0560 s, 0.0574 s, 0.0499 s), respectively.

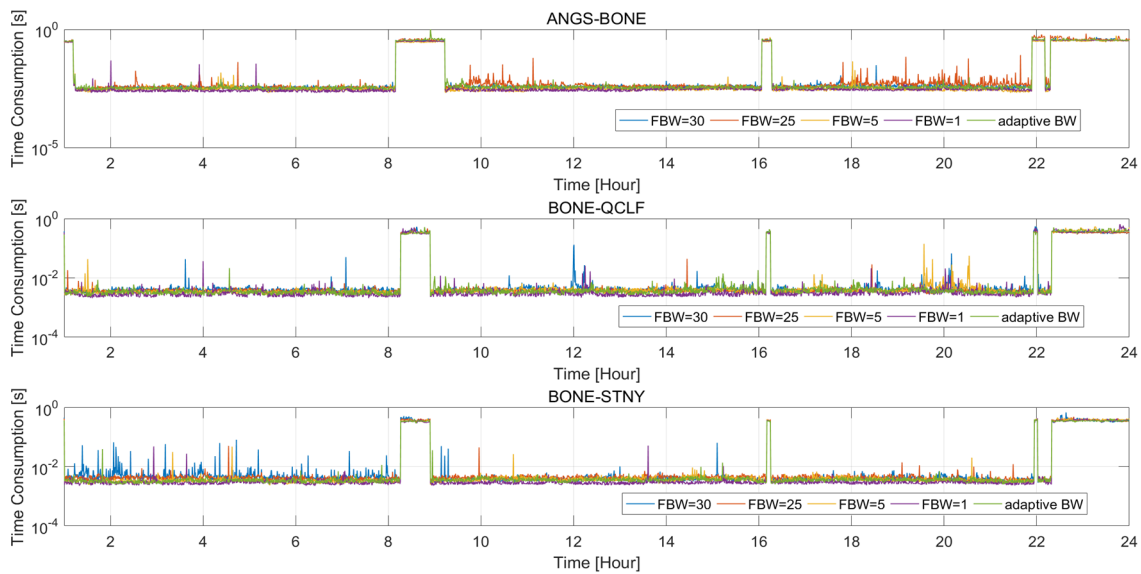


Figure 5. Time consumption with different KBW strategies on ANGS-BONE, BONE-QCLF, BONE-STNY.

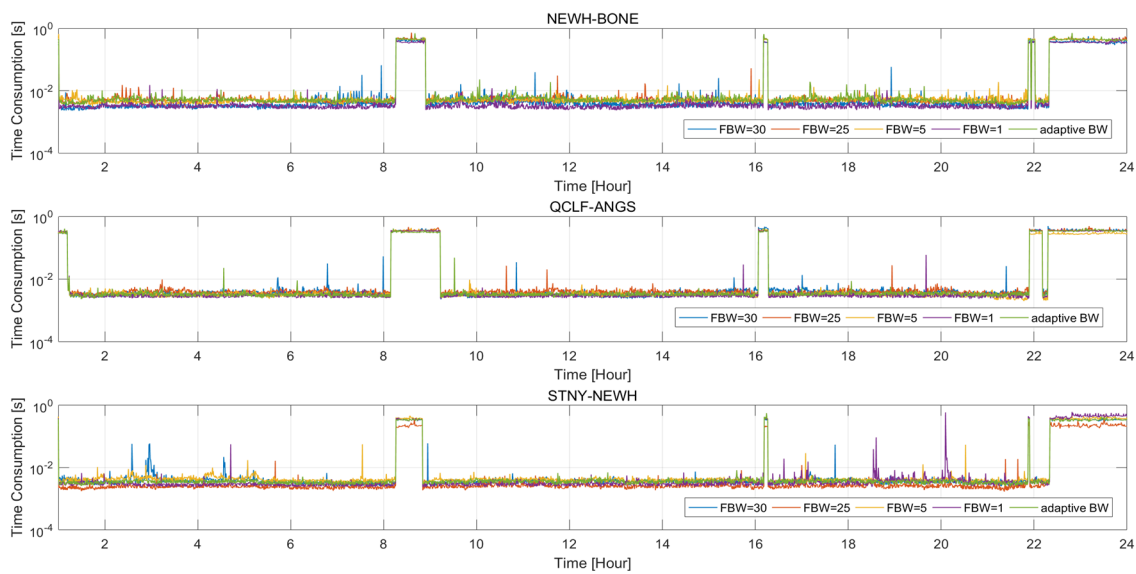


Figure 6. Time consumption with different KBW strategies on NEWH-BONE, QCLF-ANGS, STNY-NEWH.

Treating adaptive KBW as the benchmark, the efficiency improvement is demonstrated in Figure 7. For all 24 cases, negative values (shown in nine cases) indicate a longer time consumption than the benchmark, and the positive values (shown in 15 cases) indicate the opposite results. In general, degradation exists in most cases; the calculation load increased by 6.54% in the other 15 cases, and 5 of them take 10% more time. Only three cases achieved more than a 10% improvement, and the remaining six cases averagely improved by 5.41%. The superiority of the adaptive KBW strategy is the most obvious in STNY-NEWH and BONE-STNY. Thus, the proposed AMC-KF and adaptive KBW strategy can generally improve filtering efficiency.

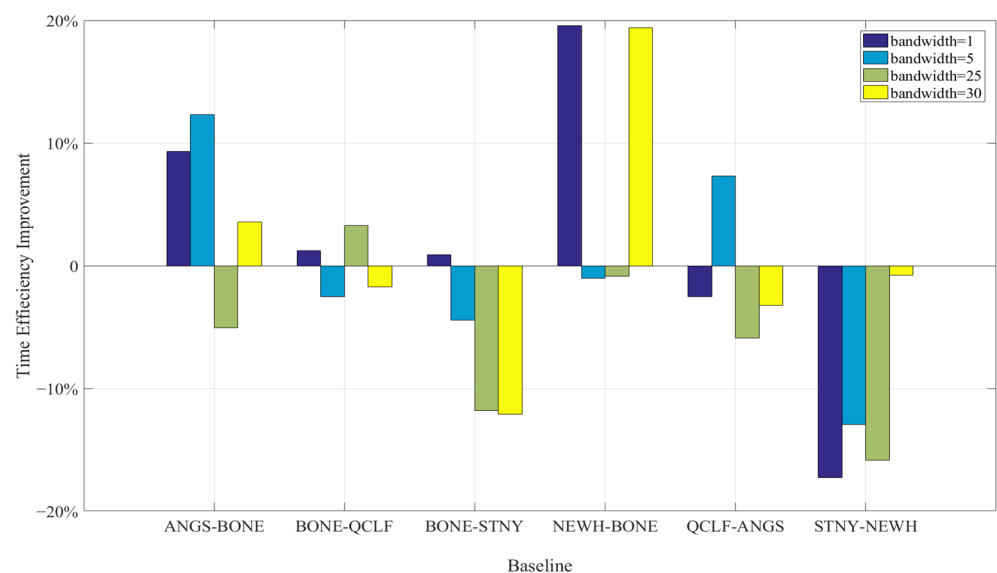


Figure 7. Time efficiency improvement for different KBW strategies.

The RMS improvement of the proposed AMC-KF compared to the original fixed KBW is shown in Figure 8. Here, the negative values mean a positioning-accuracy degradation compared to the adaptive KBW strategy.

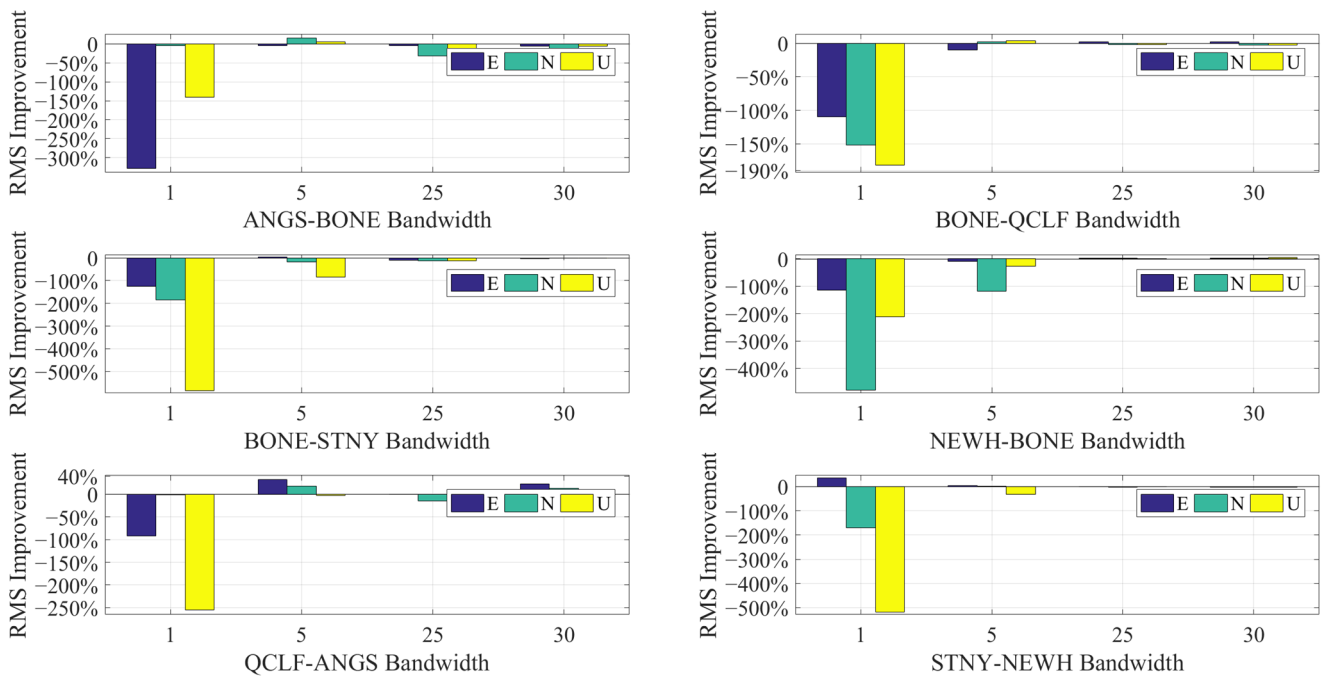


Figure 8. RMS improvement on each baseline.

The RMS increases significantly at least on one direction component while KBW = 1 and 5. Especially, the RMS on U deteriorated by almost six times (−584.261%) compared to the adaptive KBW. However, no significant performance fluctuation appears when the fixed KBW = 25 and 30, except for the −43.13% degradation on U (KBW = 25) and the 23.3% improvement on E (KBW = 30), which both occur on QCLF-ANGS.

Although the large KBW seems better, the improvement is hardly permitted as the increase in KBW amplifies the time consumption and positioning errors. In conclusion, the proposed AMC-KF method takes both efficiency and accuracy into account and is more progressive than the traditional methods with KBW fixed.

4.3. Ambiguity Resolution Analysis

In the triangle network formed by BONE-STNY-NEWH, all baselines shared the common pivot satellite, and the closure residual of DD ambiguities should meet the following constraint: $\nabla\Delta N_{\text{closure}} = \nabla\Delta N_{\text{BONE-STNY}} + \nabla\Delta N_{\text{STNY-NEWH}} + \nabla\Delta N_{\text{NEWH-BONE}} = 0$. Thus, $\nabla\Delta N_{\text{closure}}$ could be used to verify the proposed DF data-aided AR method. It should be noted that only DF data from GPS is used for a long baseline test since only GPS signal is stably received.

To illustrate the reasonability for setting the window width of the moving average to be five epochs, Figure 9 gives the differential residuals of adjacent $\nabla\Delta N_w$ on each baseline. The statics of results are shown in Table 3 and the results within ± 1 cycle are shown for easy observation. The threshold of ± 0.1 cycles, ± 0.15 cycles, and ± 0.5 cycles are also illustrated as limitations bounds.

Table 3. $\nabla\Delta N_w$ statistics of the triangle closure network.

Baseline	(−0.1, 0.1)	(−0.15, 0.15)	(0.5, 0.5)	Others
BONE_STNY	98.6679%	98.7700%	99.0339%	0.9661%
NEWH_BONE	98.3097%	98.5279%	98.9901%	1.0099%
STNY_NEWH	98.8000%	98.8726%	99.1373%	0.8627%

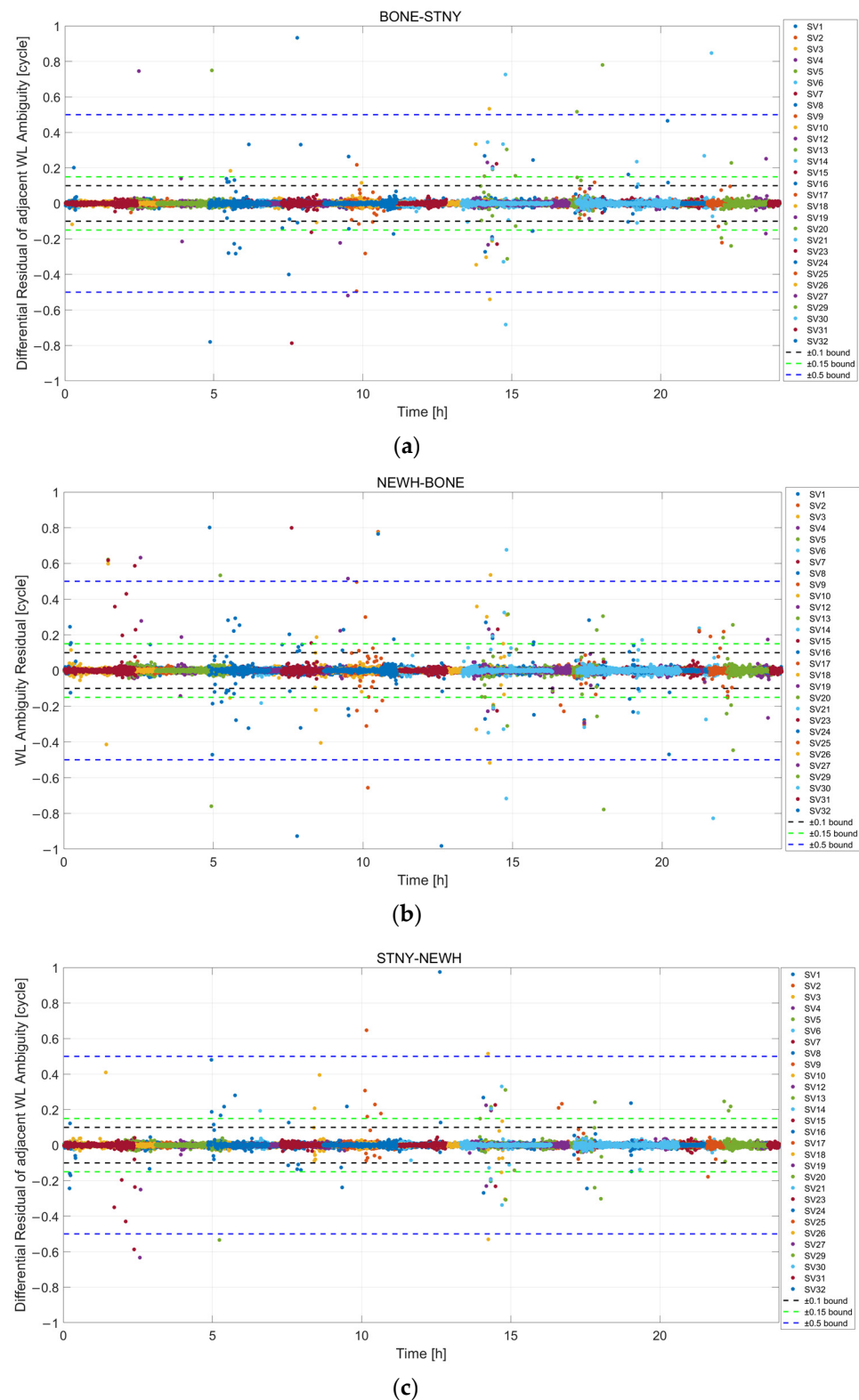


Figure 9. The $\nabla \Delta N_w$ for each baseline of the triangle closure network. (a) BONE-STNY; (b) NEWH-BONE; (c) STNY-NEWH.

In Table 3, the proportion of residuals suppressed within ± 0.1 cycles is 98.6679% for BONE-STNY, 98.3097% for NEWH-BONE, and 98.8000% for STNY-NEWH, respectively. Meanwhile, the results increase slightly when the threshold bounds increase. Thus, set-

ting the threshold to 0.1 cycles is reasonable and conservative, as most validated epochs are included.

The $\nabla\Delta N_{\text{closure}}$ of all available satellites is shown in Figure 10. It could be found that, for most satellites, the $\nabla\Delta N_{\text{closure}}$ converges to 0 once they are used and $\nabla\Delta N_{\text{closure}} = 0$ accounts for the majority. This means that $\nabla\Delta N_{\text{BONE-STNY}}$, $\nabla\Delta N_{\text{STNY-NEWH}}$, $\nabla\Delta N_{\text{NEWH-BONE}}$ are fixed correctly without initialization. The outliers usually appeared at discrete epochs contaminated by cycle slip and could be further eliminated by refined data synchronization and cycle-slip detection.

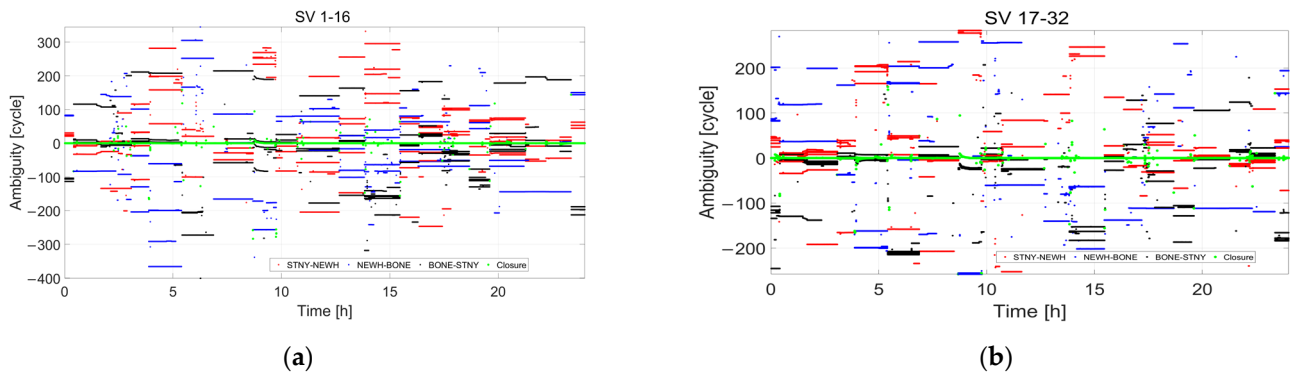


Figure 10. $\nabla\Delta N_{\text{closure}}$ in the network. (a) $\nabla\Delta N_{\text{closure}}$ for SV1-SV16; (b) $\nabla\Delta N_{\text{closure}}$ for SV17-SV32.

Figure 11 shows the detailed results of $\nabla\Delta N_{\text{closure}}$ with a total of 23377 effective epochs used. The minimum and maximum outliers accompanied by the cycle slip are (−283.56 cycles, 365.86 cycles). According to Table 4, the $\nabla\Delta N_{\text{closure}} < 0.5$ cycles in most epochs, meaning that the $\nabla\Delta N_w$ can be correctly fixed by integer rounding with a success rate of not less than 93%. The 1.7154% epochs fall into 0.5–1 cycles and 2.7848% fall into 1–5 cycles are treated as small residuals and could be improved by synchronization and cycle-slip repair. However, at least one of the three baselines fails to fix its ambiguity for the remaining 1.6041% of epochs that include residuals larger than 10 cycles. Once the $\nabla\Delta N_w$ is fixed, the corrected $\nabla\Delta\varphi$ is used for the float solution, which is expected to be with a small variance.

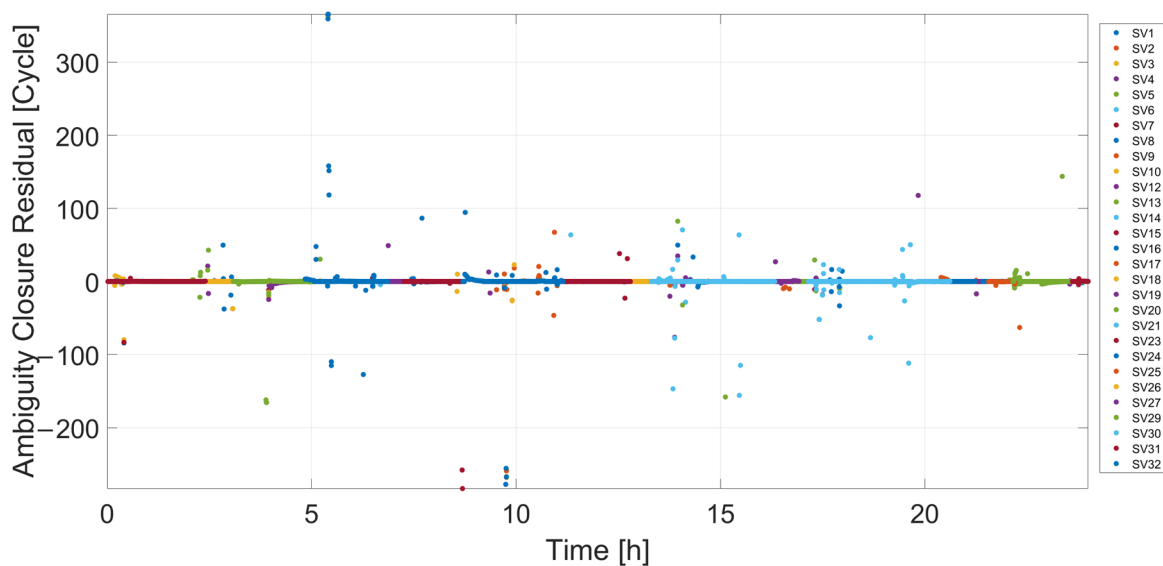


Figure 11. Ambiguity closure residual in the network.

Table 4. The statistics of $\nabla\Delta N_{\text{closure}}$.

$\nabla\Delta N_{\text{closure}}$	Residual Range (Cycle)				
	[0, 0.5)	[0.5, 1)	[1, 5)	[5, 10)	[10, +∞)
Proportion	93.1043%	1.7154%	2.7848%	0.7914%	1.6041%

The BONE-GSBN and BONE-GSBN with the distance of 106.877 km and 58.942 km, respectively, are used for the long baseline test. The improvements are both benefiting from the ‘DF Data-aid AR stage’ and the ‘filter stage’. Figure 12 and Table 5 show the positioning error on ENU components. The AMC-KF maintains the positioning error around 0 and no obvious difference occurs in all directions.

It can be inferred the proposed filter strategy suppresses the noise in DD measurements on the whole, as the correntropy can measure the similarity between the random variables through PDF.

For AMC-KF, the RMS is improved by (+78.60%, +88.85%, +77.74%) at BONE-WBEE and (+57.49%, +69.52%, +42.31%) at BONE-GSBN than DD-KF. The STD is improved by (+64.97%, +66.26%, +60.81%) at BONE-WBEE and (+51.10%, +46.89%, +40.34%) at BONE-GSBN, respectively. The proposed filter strategy can reduce the positioning error significantly for the long baseline.

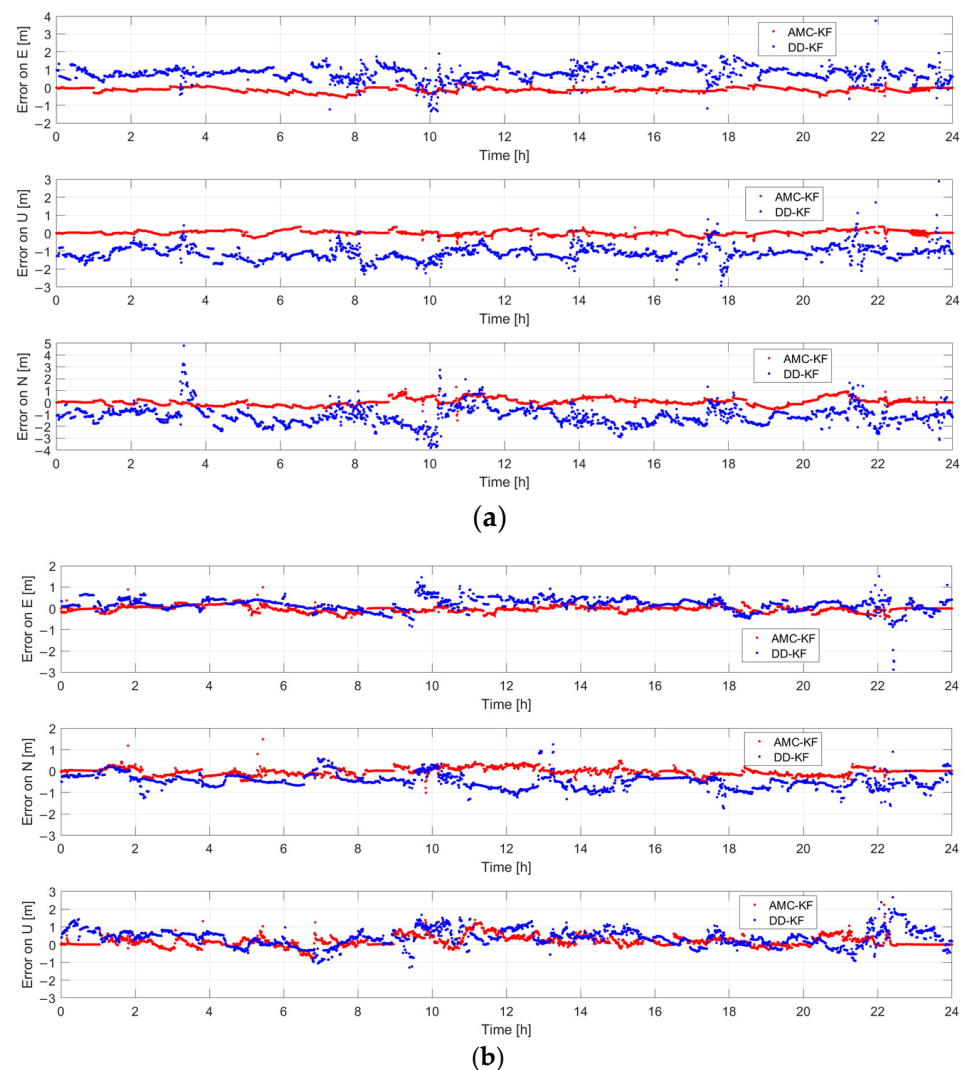
**Figure 12.** Positioning error on ENU. (a) Positioning error of BONE-WBEE; (b) positioning error of BONE-GSBN.

Table 5. The RMS and STD of position error on the ENU component.

Baseline	Model	RMS (m)			STD (m)		
		E	N	U	E	N	U
BONE-WBEE	DD-KF	0.87648	1.17600	1.38090	0.37734	0.37925	0.76978
	AMC-KF	0.18754	0.13117	0.30743	0.13217	0.12794	0.30166
BONE-GSBN	DD-KF	0.34605	0.58798	0.62407	0.29501	0.33371	0.50501
	AMC-KF	0.14710	0.17921	0.36000	0.14426	0.17722	0.30130

5. Conclusions

In terms of the timeliness and accuracy of RTK in harsh environments, both the measurement quality and the filter robustness need to improve, especially with the presence of non-Gaussian noise. This paper focus on multi-GNSS DF applications and a new nonlinear filter strategy is proposed. It consists of the DF data-aided AR method and the AMC-KF based on MCC and adaptive KBW. The superiorities are verified through tests with various baselines. First of all, ionosphere-free and wide-lane measurements are used for the DF data-aided AR method. The ambiguities on each frequency are directly converted without searching. Then, the corrected carrier measurements are used for the float solution by the proposed AMC-KF. The AMC-KF is robust to non-Gaussian noise and sparking noise as it employs MCC and adaptive KBW to measure the similarity between the input and output. Compared to the conventional DD-KF, the proposed strategy achieves higher accuracy and efficiency. The following conclusions are obtained:

- (1) For the positioning accuracy of short baselines, the RMS and STD of positioning error improved by more than 30%, 30%, and 60% on the E, N, and U components, respectively. The applicability and flexibility of the proposed AMC-KF are validated significantly.
- (2) For the proposed adaptive KBW, the efficiency and accuracy are compared and validated with fixed KBW (1, 5, 25, 30). The results show that large KBWs increase the computational load, while the small KBWs gain a worse positioning accuracy. The proposed optimization strategy can change the KBW adaptively according to the measurements and is validated to be effective as it considers both efficiency and accuracy.
- (3) A total of 29 satellites were involved in the ambiguity resolution test with long baselines. It validates that the proposed DF data-aided AR method achieves a success rate of more than 93%. The results are expected to be further improved with stringent data synchronization and cycle-slip detection.
- (4) For the long baseline test, the proposed filter strategy obtains an improvement of more than 40% in all directions as the noise is effectively suppressed. For the longer baseline BONE-WBEE, the RMS of positioning error is reduced by more than 75% on E, N, and U, which shows that the proposed method plays a better role in long baseline RTK when the multi-GNSS multi-frequency data is stably available.

Our future work focuses on deriving the sequential form of the proposed nonlinear filter strategy and applying it to smartphone RTK applications. To improve the precision and reliability of dynamic navigation in urban environments, the integration of the proposed method with vector-tracking GNSS receivers will also be explored.

Author Contributions: Conceptualization, J.L.; methodology, J.L.; software, J.L. and T.L.; investigation, Y.J., B.X., and Z.L.; data curation, J.L., M.S. and T.L.; writing—original draft preparation, J.L.; writing—review and editing, B.X., M.S., M.L., Z.L. and G.X.; supervision, Y.J., B.X., Z.L., and G.X. All authors have read and agreed to the published version of the manuscript.

Funding: This study is supported by the Guangdong Basic and Applied Basic Research Foundation (No. 2021A1515012600); the Opening Project of Guangxi Wireless Broadband Communication and Signal Processing Key Laboratory (No. GXKL06200217); the Open Fund of Key Laboratory of Urban Land Resources Monitoring and Simulation, Ministry of Natural Resources (No. KF-2021-06-104).

Data Availability Statement: The authors are grateful to the Global Navigation Satellite System Data Centre of Australia for publicly sharing their GNSS data.

Acknowledgments: We are grateful to the anonymous reviewers and editors for their helpful and constructive suggestions, which significantly improved the quality of the paper.

Conflicts of Interest: The authors declare no conflict of interest.

Appendix A

Defining the common geometry distance $\rho + c(\delta t_u - \delta t^s) + T$ without considering ionosphere delay as Θ . The carrier phase measurement φ (in cycles) with wavelength λ and code measurements P (in meters) are defined as follows:

$$\begin{cases} \varphi_1 = \frac{f_1}{c}\Theta - \frac{A}{cf_1} + N_1 + \zeta_{\varphi_1} \\ \varphi_2 = \frac{f_2}{c}\Theta - \frac{A}{cf_2} + N_2 + \zeta_{\varphi_2} \\ P_1 = \Theta + \frac{A}{f_1^2} + \varepsilon_{P_1} \\ P_2 = \Theta + \frac{A}{f_2^2} + \varepsilon_{P_2} \end{cases} \quad (\text{A1})$$

where f_1 and f_2 represent different frequencies, t_u and t^s are the clock errors from the user receiver and satellite and ζ and ε are the unmodelled noise on φ and P . The c denotes the speed of light. The Θ and A can be expressed by P_1 and P_2 as follows:

$$A = \frac{f_1^2 f_2^2 [(P_1 - P_2) - (\varepsilon_{P_1} - \varepsilon_{P_2})]}{f_2^2 - f_1^2} = \frac{f_1^2 f_2^2 (P_1 - P_2)}{f_2^2 - f_1^2} + \varepsilon_A \quad (\text{A2})$$

$$\Theta = \frac{(f_1^2 P_1 - f_2^2 P_2) - (f_1^2 \varepsilon_{P_1} - f_2^2 \varepsilon_{P_2})}{f_1^2 - f_2^2} = \frac{f_1^2 P_1 - f_2^2 P_2}{f_1^2 - f_2^2} + \varepsilon_{\Theta} \quad (\text{A3})$$

where, $\varepsilon_A = \frac{f_1^2 f_2^2 (\varepsilon_{P_1} - \varepsilon_{P_2})}{f_2^2 - f_1^2}$ and $\varepsilon_{\Theta} = \frac{(f_2^2 \varepsilon_{P_2} - f_1^2 \varepsilon_{P_1})}{f_1^2 - f_2^2}$ are the noise on A and Θ , respectively. The wide-lane combination of φ is expressed as:

$$\varphi_{WL} = \varphi_1 - \varphi_2 = \left(\frac{f_1}{c} - \frac{f_2}{c} \right) \Theta - \left(\frac{f_2 - f_1}{cf_1 f_2} \right) A + N_w + \zeta_w \quad (\text{A4})$$

where N_w is the wide-lane ambiguity, $\zeta_w = (\zeta_1 - \zeta_2)$. Then, the following expression can be obtained:

$$\begin{aligned} \varphi_{WL} &= \frac{f_1 - f_2}{c} \cdot \frac{f_1^2 P_1 - f_2^2 P_2}{f_1^2 - f_2^2} - \left(\frac{f_2 - f_1}{cf_1 f_2} \right) \cdot \frac{f_1^2 f_2^2 (P_1 - P_2)}{f_2^2 - f_1^2} + N_w + \varepsilon \\ &= \frac{f_1^2 P_1 - f_2^2 P_2}{\lambda_w (f_1^2 - f_2^2)} + \left(\frac{f_1 - f_2}{cf_1 f_2} \right) \cdot \frac{f_1^2 f_2^2 (P_1 - P_2)}{f_2^2 - f_1^2} + N_w + \varepsilon \\ &= \frac{f_1^2 P_1 - f_2^2 P_2}{\lambda_w (f_1^2 - f_2^2)} + \frac{f_1 f_2 (P_1 - P_2)}{\lambda_w (f_2^2 - f_1^2)} + N_w + \varepsilon \\ &= \frac{(f_1^2 P_1 - f_2^2 P_2) - f_1 f_2 (P_1 - P_2)}{\lambda_w (f_1^2 - f_2^2)} + N_w + \varepsilon \\ &= \frac{(f_1 P_1 + f_2 P_2)}{\lambda_w (f_1 + f_2)} + N_w + \varepsilon \end{aligned}$$

where ε is the combination of the noise terms which can be expressed as $\varepsilon = \zeta_w + \left(\frac{f_1}{c} - \frac{f_2}{c} \right) \varepsilon_{\Theta} - \frac{f_2 - f_1}{cf_1 f_2} \varepsilon_A$. Finally, the N_w can be obtained as follows:

$$N_{WL} = (\varphi_1 - \varphi_2) - \frac{(f_1 P_1 + f_2 P_2)}{\lambda_w (f_1 + f_2)} + \varepsilon \quad (\text{A5})$$

In addition, the corresponding DD wide-lane ambiguity can be obtained by:

$$\nabla\Delta N_w = (\nabla\Delta\varphi_1 - \nabla\Delta\varphi_2) - \frac{(f_1\nabla\Delta P_1 + f_2\nabla\Delta P_2)}{\lambda_w(f_1 + f_2)} + \nabla\Delta\varepsilon \quad (\text{A6})$$

Appendix B

According to Equation (5), the ionosphere-free measurement is defined as $\nabla\Delta\varphi_{IF} = m\nabla\Delta\rho_1 - n\nabla\Delta\rho_2$. Where $m = \frac{f_1^2}{f_1^2 - f_2^2}$ and $n = \frac{f_2^2}{f_1^2 - f_2^2}$, the definition of symbols and variables stay the same as those above. Thus, we have the following expansion:

$$\begin{aligned} \nabla\Delta\varphi_{IF} &= m \left[\nabla\Delta\varphi_1 + \nabla\Delta N_1\lambda_1 - \frac{A}{f_1} \right] - n \left[\nabla\Delta\varphi_2 + \nabla\Delta N_2\lambda_2 - \frac{A}{f_2} \right] \\ &= m\nabla\Delta\varphi_1 + m\nabla\Delta N_1\lambda_1 - n\nabla\Delta\varphi_2 - n\nabla\Delta N_2\lambda_2 \\ &= m\nabla\Delta\varphi_1 - n\nabla\Delta\varphi_2 + m\lambda_1\nabla\Delta N_1 - n\lambda_2(\nabla\Delta N_1 - \nabla\Delta N_w) \\ &= m\nabla\Delta\varphi_1 - n\nabla\Delta\varphi_2 + m\lambda_1\nabla\Delta N_1 - n\lambda_2\nabla\Delta N_1 + n\lambda_2\nabla\Delta N_w \\ &= m\nabla\Delta\varphi_1 - n\nabla\Delta\varphi_2 + (m\lambda_1 - n\lambda_2)\nabla\Delta N_1 + n\lambda_2\nabla\Delta N_w \end{aligned}$$

In addition, then, we have

$$\begin{aligned} (m\lambda_1 - n\lambda_2)\nabla\Delta N_1 &= \nabla\Delta\varphi_{IF} - m\nabla\Delta\varphi_1 + n\nabla\Delta\varphi_2 - n\lambda_2\nabla\Delta N_w \\ \nabla\Delta N_1 &= \frac{1}{m\lambda_1 - n\lambda_2} [\nabla\Delta\varphi_{IF} - m\nabla\Delta\varphi_1 + n\nabla\Delta\varphi_2 - n\lambda_2\nabla\Delta N_w] \end{aligned}$$

References

- Liu, J.; Zhang, B.; Liu, T.; Xu, G.; Ji, Y.; Sun, M.; Nie, W.; He, Y. An efficient UD factorization implementation of Kalman filter for RTK based on equivalent principle. *Remote Sens.* **2022**, *14*, 967. [\[CrossRef\]](#)
- Zhang, K.; Jiao, W.; Wang, L.; Li, Z.; Zhou, K. Smart-RTK: Multi-GNSS kinematic positioning approach on Android smart devices with doppler-smoothed-code filter and constant acceleration model. *Adv. Space Res.* **2019**, *64*, 1662–1674. [\[CrossRef\]](#)
- Deng, C.; Tang, W.; Liu, J.; Shi, C. Reliable single-epoch ambiguity resolution for short baselines using combined GPS/BeiDou system. *GPS Solut.* **2014**, *18*, 375–386. [\[CrossRef\]](#)
- Sun, Q.; Xia, J.; Foster, J.; Falkmer, T.; Lee, H. Pursuing precise vehicle movement trajectory in urban residential area using multi-GNSS RTK tracking. *Transp. Res. Procedia* **2017**, *25*, 2361–2376. [\[CrossRef\]](#)
- Atz, M.F.; Konukseven, C.; Sermet, T.C.; Alay, S. Comparative analysis of the performance of Multi-GNSS RTK: A case study in Turkey. *Int. J. Eng. Geosci.* **2022**, *7*, 67–80. [\[CrossRef\]](#)
- Al-Shaery, A.; Zhang, S.; Lim, S.; Rizos, C. *Multi-GNSS Opportunities and Challenges*; Pres at the EGU General Assembly; European Geosciences Union: Vienna, Austria, 2012.
- Deng, C.; Liu, Q.; Zou, X.; Tang, W.; Cui, J.; Wang, Y.; Guo, C. Investigation of tightly combined single-frequency and single-epoch precise positioning using multi-GNSS data. *Remote Sens.* **2020**, *12*, 285. [\[CrossRef\]](#)
- Chen, C.; Chang, G. PPPLib: An open-source software for precise point positioning using GPS, BeiDou, Galileo, GLONASS, and QZSS with multi-frequency observations. *GPS Solut.* **2021**, *25*, 18. [\[CrossRef\]](#)
- Ibrahim, A.S.; Yacoub, A.M.; Aloji, D.N. A 3-dimensional multiband antenna for vehicular 5G sub-6 GHz/GNSS/V2X applications. *Int. J. Antennas Propag.* **2022**, *2022*, 5609110. [\[CrossRef\]](#)
- Li, X.; Wang, H.; Li, S.; Feng, S.; Wang, X.; Liao, J. GIL: A tightly coupled GNSS PPP/INS/LiDAR method for precise vehicle navigation. *Satell. Navig.* **2021**, *2*, 26. [\[CrossRef\]](#)
- Bai, L.; Sun, C.; Dempster, A.G.; Zhao, H.; Cheong, J.W.; Feng, W. GNSS-5G hybrid positioning based on multi-rate measurements fusion and proactive measurement uncertainty prediction. *IEEE Trans. Instrum. Meas.* **2022**, *71*, 8501415. [\[CrossRef\]](#)
- Xin, S.; Geng, J.; Zeng, R.; Zhang, Q.; Ortega-Culaciati, F.; Wang, T. In-situ real-time seismogeodesy by integrating multi-GNSS and accelerometers. *Measurement* **2021**, *179*, 109453. [\[CrossRef\]](#)
- Vagle, N.; Broumandan, A.; Lachapelle, G. Multiantenna GNSS and inertial sensors/odometer coupling for robust vehicular navigation. *IEEE Internet Things J.* **2018**, *5*, 4816–4828. [\[CrossRef\]](#)
- Bonnor, N. Principles of GNSS, inertial, and multisensor integrated navigation systems—Second Edition Paul D. Groves Artech House, 2013, 776 pp ISBN-13: 978-1-60807-005-3. *J. Navig.* **2014**, *67*, 191–192. [\[CrossRef\]](#)
- Broumandan, A.; Lachapelle, G. Spoofing detection using GNSS/INS/Odometer coupling for vehicular navigation. *Sensors* **2018**, *18*, 1305. [\[CrossRef\]](#)
- Odijk, D.; Teunissen, P. Characterization of between-receiver GPS-Galileo inter-system biases and their effect on mixed ambiguity resolution. *GPS Solut.* **2013**, *17*, 521–533. [\[CrossRef\]](#)
- Gao, W.; Pan, S.; Gao, C.; Wang, Q.; Shang, R. Tightly combined GPS and GLONASS for RTK positioning with consideration of differential inter-system phase bias. *Meas. Sci. Technol.* **2019**, *30*, 054001. [\[CrossRef\]](#)

18. Li, X.; Wang, B.; Li, X.; Huang, J.; Lyu, H.; Han, X. Principle and performance of multi-frequency and multi-GNSS PPP-RTK. *Satell. Navig.* **2022**, *3*, 7. [[CrossRef](#)]
19. Liu, T.; Zhang, B. Estimation of code observation-specific biases (OSBs) for the modernized multi-frequency and multi-GNSS signals: An undifferenced and uncombined approach. *J. Geod.* **2021**, *95*, 97. [[CrossRef](#)]
20. Psychas, D. Fast and Reliable Multi-GNSS Precise Point Positioning with Integer Ambiguity Resolution. Ph.D. Thesis, Delft University of Technology, Delft, The Netherlands, January 2022.
21. Zhang, G.; Xu, P.; Xu, H.; Hsu, L.-T. Prediction on the urban GNSS measurement uncertainty based on deep learning networks with long short-term memory. *IEEE Sens. J.* **2021**, *21*, 20563–20577. [[CrossRef](#)]
22. Smola, A.; Gretton, A.; Le, S.; Schlkopf, B. A hilbert space embedding for distributions. In Proceedings of the International Conference on Algorithmic Learning Theory, Sendai, Japan, 1–4 October 2007.
23. Li, T.; Zhang, H.; Gao, Z.; Chen, Q.; Niu, X. High-accuracy positioning in urban environments using single-frequency multi-GNSS RTK/MEMS-IMU integration. *Remote Sens.* **2018**, *10*, 205. [[CrossRef](#)]
24. Gong, X.; Zheng, F.; Gu, S.; Zhang, Z.; Lou, Y. The long-term characteristics of GNSS signal distortion biases and their empirical corrections. *GPS Solut.* **2022**, *26*, 52. [[CrossRef](#)]
25. Chen, B.; Wang, X.; Li, Y.; Principe, J.C. Maximum correntropy criterion with variable center. *IEEE Signal Process. Lett.* **2019**, *26*, 1212–1216. [[CrossRef](#)]
26. Zhang, J.; Liu, Y.; Liu, H.; Wang, J. Learning local–global multiple correlation filters for robust visual tracking with Kalman filter redetection. *Sensors* **2021**, *21*, 1129. [[CrossRef](#)]
27. Valipour, M.; Ricardez-Sandoval, L.A. Abridged Gaussian sum extended Kalman filter for nonlinear state estimation under non-Gaussian process uncertainties. *Comput. Chem. Eng.* **2021**, *155*, 107534. [[CrossRef](#)]
28. Wang, H.; Zhang, W.; Zuo, J.; Wang, H. Outlier-robust Kalman filters with mixture correntropy. *J. Franklin Inst.* **2020**, *357*, 5058–5072. [[CrossRef](#)]
29. Sahnoudi, M.; Landry, R. A nonlinear filtering approach for robust multi-GNSS RTK positioning in presence of multipath and ionospheric delays. *IEEE J. Sel. Top. Signal Process.* **2009**, *3*, 764–776. [[CrossRef](#)]
30. Flores, T.K.S.; Villanueva, J.M.M.; Gomes, H.P.; Catunda, S.Y.C. Adaptive pressure control system based on the maximum correntropy criterion. *Sensors* **2021**, *21*, 5156. [[CrossRef](#)] [[PubMed](#)]
31. Hu, C.; Wang, G.; Ho, K.; Liang, J. Robust ellipse fitting with Laplacian kernel based maximum correntropy criterion. *IEEE Trans. Image Process.* **2021**, *30*, 3127–3141. [[CrossRef](#)]
32. Xiong, W.; Schindelbauer, C.; So, H.C.; Wang, Z. Maximum correntropy criterion for robust TOA-based localization in NLOS environments. *Circuits Syst. Signal Process.* **2021**, *40*, 6325–6339. [[CrossRef](#)]
33. Zhao, H.; Liu, D.; Lv, S. Robust maximum correntropy criterion subband adaptive filter algorithm for impulsive noise and noisy input. *IEEE Trans. Circuits Syst. II Express Briefs* **2021**, *69*, 604–608. [[CrossRef](#)]
34. Fakoorian, S.; Santamaria-Navarro, A.; Lopez, B.T.; Simon, D.; Agha-mohammadi, A.-A. Towards robust state estimation by boosting the maximum correntropy criterion Kalman filter with adaptive behaviors. *IEEE Robot. Autom. Lett.* **2021**, *6*, 5469–5476. [[CrossRef](#)]
35. Fan, X.; Wang, G.; Han, J.; Wang, Y. Interacting multiple model based on maximum correntropy Kalman filter. *IEEE Trans. Circuits Syst. II Express Briefs* **2021**, *68*, 3017–3021. [[CrossRef](#)]
36. Zhao, W.; Zhao, H.; Liu, L. A single beacon-aided cooperative localization algorithm based on maximum correntropy criterion. In Proceedings of the 2021 International Wireless Communications and Mobile Computing (IWCMC), Harbin, China, 28 June–2 July 2021; pp. 1835–1839.
37. Chen, B.; Xing, L.; Zhao, H.; Xu, B.; Principe, J.C. Robustness of maximum correntropy estimation against large outliers. *arXiv* **2017**, arXiv:1703.08065.
38. Odolinski, R.; Teunissen, P.; Odijk, D. Combined BDS, Galileo, QZSS and GPS single-frequency RTK. *GPS Solut.* **2015**, *19*, 151–163. [[CrossRef](#)]
39. Wang, J.; Xu, T.; Nie, W.; Xu, G. A simplified processing algorithm for multi-baseline RTK positioning in urban environments. *Measurement* **2021**, *179*, 109446. [[CrossRef](#)]
40. Chen, P.; Ma, Y.; Liu, H.; Zheng, N. A new global tropospheric delay model considering the spatiotemporal variation characteristics of ZTD with altitude coefficient. *Earth Space Sci.* **2020**, *7*, e2019EA000888. [[CrossRef](#)]
41. Lai, C.; Guo, R. Extend the RTK survey to GNSS-denied areas using a low-cost inertial-aided positioning pole. In Proceedings of the 34th International Technical Meeting of the Satellite Division of The Institute of Navigation (ION GNSS+ 2021), St. Louis, MO, USA, 20–24 September 2021; pp. 3212–3226.
42. Liu, Y.; Gao, Z.; Xu, Q.; Li, Y.; Chen, L. Assessing partial ambiguity resolution and WZTD-constraint multi-frequency RTK in an urban environment using new BDS signals. *GPS Solut.* **2022**, *26*, 88. [[CrossRef](#)]
43. Miwa, M.; Ushiroda, T. Precision flight drones with RTK-GNSS. *J. Robot. Mechatron.* **2021**, *33*, 371–378. [[CrossRef](#)]
44. Xue, X.; Qin, H.; Lu, H. High-precision time synchronization of kinematic navigation system using GNSS RTK differential carrier phase time transfer. *Measurement* **2021**, *176*, 109132. [[CrossRef](#)]
45. Roberts, G.W.; Tang, X.; Brown, C.J. Measurement and correlation of displacements on the Severn Suspension Bridge using GPS. *Appl. Geomat.* **2018**, *11*, 161–176. [[CrossRef](#)]
46. Teunissen, P. Towards a unified theory of GNSS ambiguity resolution. *J. Glob. Position. Syst.* **2003**, *2*, 1–12. [[CrossRef](#)]

47. Singh, A.; Principe, J.C. Using Correntropy as a cost function in linear adaptive filters. In Proceedings of the 2009 International Joint Conference on Neural Networks, Atlanta, GA, USA, 14–19 June 2009.
48. Chen, B.; Xing, L.; Zhao, H.; Du, S.; Principe, J.C. Effects of outliers on the maximum correntropy estimation: A robustness analysis. *IEEE Trans. Syst. Man Cybern. Syst.* **2019**, *51*, 4007–4012. [[CrossRef](#)]
49. Lu, L.; Zhao, H. Active impulsive noise control using maximum correntropy with adaptive kernel size. *Mech. Syst. Signal Process.* **2017**, *87*, 180–191. [[CrossRef](#)]
50. Cinar, G.T.; Principe, J.C. Hidden state estimation using the Correntropy Filter with fixed point update and adaptive kernel size. In Proceedings of the 2012 International Joint Conference on Neural Networks (IJCNN), Brisbane, Australia, 10–15 June 2012.
51. Chen, B.; Liu, X.; Zhao, H.; Principe, J.C. Maximum correntropy Kalman filter. *Automatica* **2017**, *76*, 70–77. [[CrossRef](#)]
52. Liu, W.; Pokharel, P.P.; Principe, J.C. Correntropy: Properties and applications in non-Gaussian signal processing. *IEEE Trans. Signal Process.* **2007**, *55*, 5286–5298. [[CrossRef](#)]
53. Izanloo, R.; Fakoorian, S.A.; Yazdi, H.S.; Dan, S. Kalman filtering based on the maximum correntropy criterion in the presence of non-Gaussian noise. In Proceedings of the 2016 Annual Conference on Information Science and Systems (CISS), Princeton, NJ, USA, 16–18 March 2016.
54. Heravi, A.R.; Hodtani, G.A. A new information theoretic relation between minimum error entropy and maximum correntropy. *IEEE Signal Process. Lett.* **2018**, *25*, 921–925. [[CrossRef](#)]
55. Fakoorian, S.; Izanloo, R.; Shamshirgaran, A.; Dan, S. Maximum correntropy criterion Kalman filter with adaptive kernel size. In Proceedings of the 2019 IEEE National Aerospace and Electronics Conference (NAECON), Dayton, OH, USA, 15–19 July 2019.
56. Botev, Z.I.; Grotowski, J.F.; Kroese, D.P. Kernel density estimation via diffusion. *Ann. Stat.* **2010**, *38*, 2916–2957. [[CrossRef](#)]
57. Hou, P.; Zhang, B.; Yasyukevich, Y.V.; Liu, T.; Zha, J. Multi-frequency phase-only PPP-RTK model applied to BeiDou data. *GPS Solut.* **2022**, *26*, 76. [[CrossRef](#)]